Title

Two-Photon Autofluorescence Imaging Reveals Cellular Structures Throughout the Retina of the Living Primate Eye.

Journal

Investigative Ophthalmology and Visual Science, 57(2)

Authors

Sharma, Robin
Williams, David
Palczewska, Grazyna
et al.

Publication Date

2016-02-01

DOI

10.1167/iovs.15-17961

Peer reviewed

Two-Photon Autofluorescence Imaging Reveals Cellular Structures Throughout the Retina of the Living Primate Eye

Robin Sharma,[1,2] David R. Williams,[1–3] Grazyna Palczewska,[4] Krzysztof Palczewski,[5] and Jennifer J. Hunter[2,3]

[1]The Institute of Optics, University of Rochester, Rochester, New York, United States
[2]Center for Visual Science, University of Rochester, Rochester, New York, United States
[3]Flaum Eye Institute, University of Rochester, Rochester, New York, United States
[4]Polgenix, Inc., Cleveland, Ohio, United States
[5]Department of Pharmacology, Cleveland Center for Membrane and Structural Biology, School of Medicine, Case Western Reserve University, Cleveland, Ohio, United States

Correspondence: Robin Sharma, University of Rochester, Center for Visual Science, 601 Elmwood Avenue, BOX 319, Rochester, NY 14642, USA; rsharma@optics.rochester.edu.

Submitted: August 15, 2015
Accepted: December 30, 2015

Citation: Sharma R, Williams DR, Palczewska G, Palczewski K, Hunter JJ. Two-photon autofluorescence imaging reveals cellular structures throughout the retina of the living primate eye. *Invest Ophthalmol Vis Sci*. 2016;57:632–646. DOI:10.1167/iovs.15-17961

Purpose. Although extrinsic fluorophores can be introduced to label specific cell types in the retina, endogenous fluorophores, such as NAD(P)H, FAD, collagen, and others, are present in all retinal layers. These molecules are a potential source of optical contrast and can enable noninvasive visualization of all cellular layers. We used a two-photon fluorescence adaptive optics scanning light ophthalmoscope (TPF-AOSLO) to explore the native autofluorescence of various cell classes spanning several layers in the unlabeled retina of a living primate eye.

Methods. Three macaques were imaged on separate occasions using a custom TPF-AOSLO. Two-photon fluorescence was evoked by pulsed light at 730 and 920 nm excitation wavelengths, while fluorescence emission was collected in the visible range from several retinal layers and different locations. Backscattered light was recorded simultaneously in confocal modality and images were postprocessed to remove eye motion.

Results. All retinal layers yielded two-photon signals and the heterogeneous distribution of fluorophores provided optical contrast. Several structural features were observed, such as autofluorescence from vessel walls, Müller cell processes in the nerve fibers, mosaics of cells in the ganglion cell and other nuclear layers of the inner retina, as well as photoreceptor and RPE layers in the outer retina.

Conclusions. This in vivo survey of two-photon autofluorescence throughout the primate retina demonstrates a wider variety of structural detail in the living eye than is available through conventional imaging methods, and broadens the use of two-photon imaging of normal and diseased eyes.

Keywords: ophthalmic imaging, Müller cells, vasculature, photoreceptors, nuclear layers

The ophthalmoscope was invented by Helmholtz[1] in 1851 and was followed by the development of fundus photography[2,3] almost three decades later. For the first time, images of the retina, optic disc, macula, and vascular structures could be recorded noninvasively in healthy and diseased eyes[4] with such cameras. More than a century later, information captured by fundus photography can be supplemented and enhanced by fluorescein angiography,[5] confocal scanning light ophthalmoscopy (cSLO),[6,7] and optical coherence tomography (OCT).[8–13] These techniques have improved the contrast for visualizing fine vascular structures, fluorescence from retinal layers, and assessment of the thickness of various retinal layers. Deployment of adaptive optics (AO) in fundus cameras,[14] cSLO,[15] and OCT[16] instruments has further improved optical resolution, thus permitting imaging of single cells, such as rods, foveal cones,[17,18] RPE cells,[19] and blood cells in small retinal vessels.[20,21] This is of interest for monitoring longitudinal changes in diseases, such as retinitis pigmentosa,[22,23] retinal dystrophy,[24–26] age-related macular degeneration,[27,28] and diabetic retinopathies,[29–31] especially since cellular scale imaging can permit semiautomated quantification of the density and spacing of these cells[32–37] as well as AO-assisted microperimetry.[38,39]

Correction of monochromatic aberrations by AO also has enhanced the contrast for gross structures, such as lamina cribrosa in the optic nerve head[40,41] and retinal nerve fiber bundles in the inner retina,[15,42,43] which are affected by diseases, such as glaucoma. However, the neural and glial cells, which are directly affected by these diseases, are largely translucent and imaging them at a fine scale in living eyes without the use of contrast agents has been a longstanding challenge. Currently, exogenous fluorophores cannot be used for imaging such neural and glial structures in human subjects due to concerns about toxicity and invasiveness. Without the use of exogenous dyes, optical contrast for cellular scale imaging of retinal structures is limited by several factors, such as the numerical aperture of the eye, light budget allowed for safe imaging, and their relative propensity to absorb, transmit, reflect, scatter, waveguide, or fluoresce light. While detection of backscattered light is the most commonly used tactic for

cellular scale AO imaging, an alternative approach for extracting intrinsic contrast from the living retina is to harness autofluorescence from endogenous fluorophores. All cells contain molecules, such as NAD(P)H, FAD, and other metabolites known to be autofluorescent.[44] Additionally, photoreceptors, Müller cells, and the RPE contain retinoids, such as retinol, retinyl esters, A2E, and lipofuscin, that also are autofluorescent.[45–48] Similarly, intrinsic fluorophores, such as collagen and elastin, are well known to be constituents of vessel walls, basement membranes, and the extracellular matrix between individual cells of the retina.[49] Not only are these molecules capable of providing structural contrast, some also are involved in cellular physiology and can serve as biomarkers of cell health.[50–52] Single-photon excitation spectra for these fluorophores lie primarily in the ultraviolet range and their fluorescence cannot be excited through the pupil of the primate eye through conventional imaging techniques because of the ocular transmission window.[53]

Two-photon excitation[54] can be used for targeting these endogenous fluorophores with near-infrared light, which is easily transmitted through the optics of the primate eye. Two-photon microscopy already has been shown to excite fluorescence from all layers in the retina from the nerve fiber layer down to the RPE in histologic preparations, providing native structural contrast for nuclear and cellular features.[55–57] These studies, along with others,[58,59] show that two-photon imaging has the potential to image cellular structures throughout the retina but is it possible to visualize these structures noninvasively in the living eye? Before this study, two-photon fluorescence adaptive optics scanning light ophthalmoscopes (TPF-AOSLOs) were used to image photoreceptors in primates[60] and labeled ganglion cells in mice.[61] To explore fluorescence from various retinal layers, we deployed a TPF-AOSLO dedicated to imaging the unlabeled primate eye and the results are described here.

Methods

Animal Preparation

Four nonhuman primates, two female Macaca rhesus monkeys (16 and 4 years old) and two male Macaca fascicularis monkeys (8 and 20 years old), were used for these experiments. Subjects were handled as per the protocols prescribed and approved by the University of Rochester's committee for animal research and in accordance with the ARVO Animal Statement for the Use of Animals in Ophthalmic and Vision Research. Ketamine (10–20 mg/kg) and Valium (0.25 mL/kg) were used initially to sedate the animals before intubation. For prolonged anesthesia, a steady dosage of isofluorane (ranging from 1%–5%) was administered, along with a paralytic dose of vecuronium (60 μg/kg/h) for periods of up to 6 hours to reduce eye movements. The average imaging session duration was <6 hours, during which the subjects were imaged intermittently. A ventilator was used to maintain breathing while subjects were placed on a custom stereotaxic cart in a sternal position. The eye being imaged was positioned at the cart's gimbal focus of rotation and held open by a lid speculum. Corneal hydration was maintained by coating the eyes with Genteal (Alcon, Fort Worth, TX, USA) and contact lenses, which also corrected the base refractive error. Eyes from one of the animals used in the in vivo study subsequently were histologically examined. Retinas were fixed in formaldehyde and two-photon microscopy (Fluoview 1000 AOM-MPM; Olympus Corporation, Center Valley, PA, USA) was done nearly 45 days after enucleation.

Two-Photon Fluorescence Adaptive Optics Scanning Light Ophthalmoscope

A custom TPF-AOSLO was designed and built to optimize the efficiency of two-photon fluorescence imaging in the living monkey eye. Details about the system design and layout have been described in another publication.[62] The system was designed to image from the nerve fiber layer to the RPE layer, over >3° field of view. All fluorescence images reported here were captured with either 730, 900, or 920 nm excitation wavelengths and corresponding reflectance images were either collected at the same wavelength as used for fluorescence excitation or at 790 nm. For imaging at 900 or 920 nm, emission was collected between 400 to 680 nm with the use of two filters with transmission windows from 400 to 680 nm (ET680SP-2P8; Chroma Technology Corporation, Bellows Falls, VT, USA). For imaging at 730 nm an additional filter with a transmission window from 400 to 550 nm (E550sp-2p; Chroma Technology Corporation) was used.

Through Focus Imaging and Axial Resolution

To evaluate the relative signal strength at different layers in the retina, through-focus image stacks were collected at several retinal locations. By manipulating the adaptive optics control algorithm, varying amounts of spherical wavefront curvature were imparted to the imaging beam by use of the deformable mirror to focus light at different layers in the retina while maintaining wavefront correction for other aberrations. This was done at $\lambda_{ex} = 730$ and 920 nm at the same retinal location in the same animal but during different sessions weeks apart (Fig. 1b). Fine vascular structures simultaneously imaged in reflectance were used to estimate the relative focus for 730 nm and 920 nm beams, and, thus, were plotted on the same scale along with the theoretical intensity point spread function (IPSF) at 920 nm based on expressions derived by Gu and Sheppard.[63,64] Additionally, a high axial resolution spectral-domain optical coherence tomography (SD-OCT) scan was collected from the same retinal location (Fig. 1a) with a Spectralis HRA+OCT (Heidelberg Engineering, Heidelberg, Germany). Distinct features in the SD-OCT scan were aligned visually to the axial depth information of their corresponding adaptive optics ophthalmic images.

Axial resolution was not determined experimentally in this study, but we estimated the theoretical axial resolution (at full-width half-maximum) to be 25 μm at 730 nm and 32 μm at 920 nm based on the expression described by Zipfel et al.[65,66] for low numerical aperture systems:

$$\omega_z = 2\sqrt{\ln 2}\frac{0.532\,\lambda}{\sqrt{2}\,NA}\left[\frac{1}{n-\sqrt{n^2-NA^2}}\right],$$

where λ is the wavelength, NA is the numerical aperture (0.22) and n is the refractive index (1.33).

Image Analysis and Processing

Real-time videos were captured at a frame rate of 20 or 22.5 Hz through custom software. The pixel clock was 35 MHz and frame size was 512 lines along the direction of the slow scanner, which had a linear motion range, and anywhere from 656 to 728 pixels along the direction of the fast scanner featuring a sinusoidal motion range. This sinusoidal motion was later corrected during postprocessing by application of a calibration desinusoiding matrix coordinate transformation to equalize the size of all pixels across the field.

Investigative Ophthalmology & Visual Science

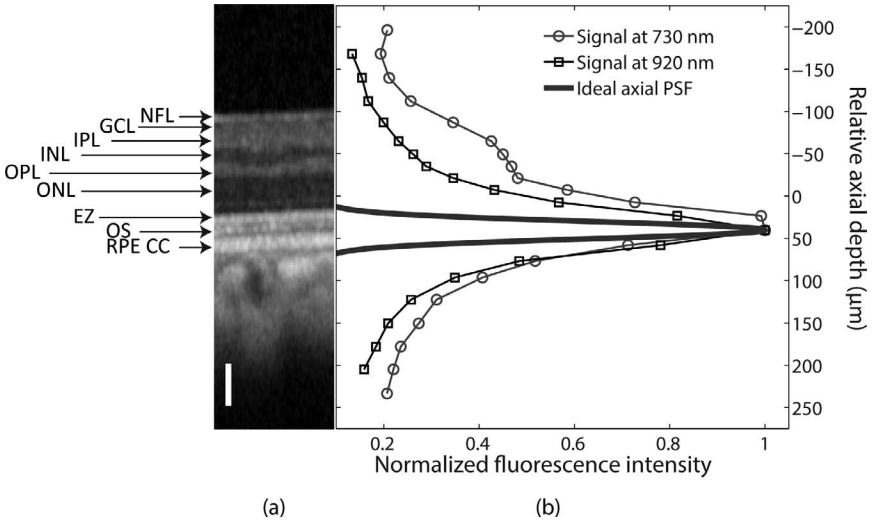

Figure 1. Relative two-photon autofluorescence levels in the primate retina. (**a**) Optical coherence tomography image of a retinal location 5 mm temporal to the fovea. *Labels* refer to the various retinal layers that can be distinguished.[104] (**b**) Two-photon autofluorescence signals plotted for 730 and 920 nm excitation. These data were collected at the same retinal location on two different imaging sessions, almost 4 weeks apart. NFL, nerve fiber layer; GCL, ganglion cell layer; IPL, inner plexiform layer; INL, inner nuclear layer; OPL, outer plexiform layer; ONL, outer nuclear layer; EZ, ellipsoid zone, outer segment junction; OS, outer segment; RPE CC, retinal pigment epithelium and choriocapillaris. *Scale bars*: 50 μm.

To account for residual motion artifacts in the videos, high contrast reflectance videos were processed through custom demotion software that calculated interframe motion with respect to a specified reference frame in the video through normalized cross-correlation measurements.[67] Many images also were generated in real-time with custom tracking and registration algorithms described in detail previously.[68] The peak of the radial average of the Fourier transform was used to estimate the average center-to-center cell spacing. The plot shown in Figure 2c was generated by rotating images shown Figures 2a and 2b using radon transform to vertically align the streaks. Then, common regions of interest were manually selected (as shown in yellow boxes, Figs. 2a, 2b) and pixels along the vertical columns were averaged to generate average cross-sectional intensities across streaks.

Results and Discussion

Two-Photon Autofluorescence as a Function of Depth in the Retina

Two-photon excited autofluorescence could be detected throughout the living primate retina and the absolute signal intensity detected per unit pixel was <1 pW. Relative autofluorescence signal levels collected at 730 and 920 nm excitation light are shown in Figure 1b along with the theoretical axial PSF at 920 nm. These curves were normalized to their peaks. For visual comparison, a high axial resolution OCT scan from the same retinal location is shown in Figure 1a. Autofluorescence was greatest from the outer retinal layers for both wavelengths and decreased as the focus was shifted to more vitreal or scleral retinal layers. For 920 nm excitation,

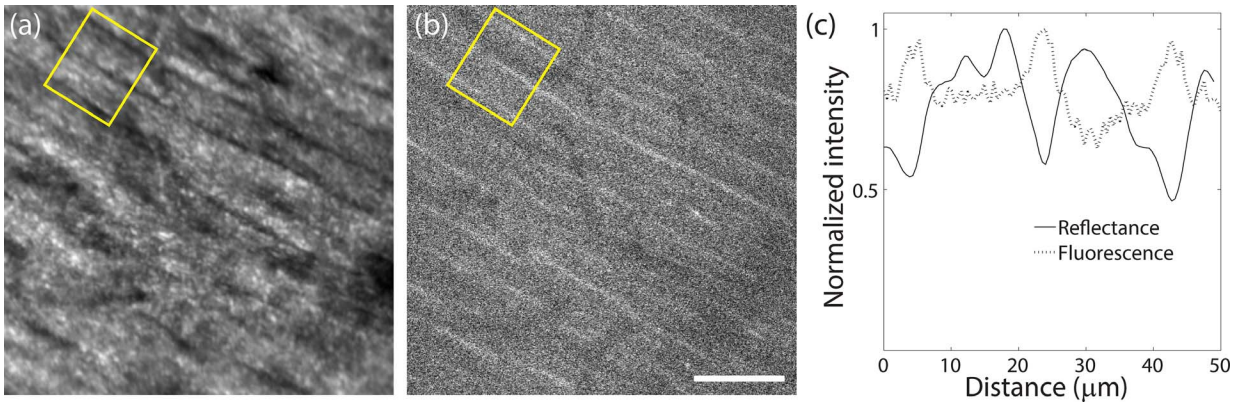

Figure 2. (**a**) Nerve fiber bundles imaged using a conventional confocal reflectance modality. Dark gaps between bundles are visible. (**b**) Two-photon fluorescence image at $\lambda_{ex} = 730$ nm, captured simultaneously. *Bright streaks* are visible in the two-photon image. (**c**) Averaged cross-section across the dark bands in (**a**) and the *bright streaks* seen in (**b**) for the locations marked by *yellow rectangles*. This shows that the dark bands in reflectance correspond to bright bands in the two photon images. Two-photon imaging conditions: average power at the cornea, 7 mW; scan size, 1.1° × 1.3°; duration of recording, 12,800 frames (582 seconds); exposure, 4823 J/cm^2. Exposure was greater than MPE by a factor of 8.5. *Scale bars*: 50 μm.

autofluorescence decreased monotonically when the two-photon excitation beam was focused at vitreal or scleral retinal layers, as shown in Figure 1. At 730 nm excitation, photoreceptors were the brightest structures imaged in the retina, although the shape of the curve was not symmetric. A shoulder was seen in the axial scan profile at focal planes corresponding to the inner retinal layers. The widths of the axial profiles for 730 and 920 nm excitation were broader than the theoretical axial PSF, perhaps because fluorescence from other layers contributed to the broadening of this profile, although residual aberrations also might broaden the axial PSF.

Two-Photon Excited Fluorescence From the Nerve Fiber Layer

Bright streak-like structures were consistently visible at various retinal locations when the excitation beam was focused at the nerve fiber layer of the inner retina. These streaks were oriented along the same direction as that of the nerve fiber bundles, which were simultaneously imaged in reflectance. Moreover, the thin, bright streaks in autofluorescence images corresponded to and overlapped with dark bands between the nerve fiber axon bundles visualized in reflectance, although not all such dark bands had corresponding bright streaks in two-photon fluorescence images. An example is shown in Figure 2b, where relatively greater autofluorescence was visible from those regions in the two-photon image that appeared relatively darker in reflectance imaging (Fig. 2a). The distances between these stripes were similar to the thickness of colocated nerve fiber bundles as shown in Figure 2c even though the alignment between reflectance and fluorescence data was limited by the radon transform, source alignment as well as by chromatic aberration. Fluorescence from bright streaks, as shown in Figure 2b, were reported previously in the nerve fiber layer of monkey and human retinas.[56,57]

At the nerve fiber layer, fluorescence from nerve fiber bundles also was visible but the source of fluorescence from the bright streaks located between the fiber bundles could be different. It is known that processes of Müller cells wrap around ganglion cell axons to form glial tunnels that package the axons into nerve fiber bundles.[69–72] Our findings are consistent with studies on two-photon imaging of freshly isolated frog retina that also have indicated that the autofluorescence from Müller cell processes is greater than that from all other cell types present in the inner retina.[55] We observed that, although nerve fibers emit fluorescence, it was comparatively weaker.

The source of autofluorescence in Müller cells is unclear. Ultrastructural imaging of Müller cells shows that their nuclei and cytoplasm are darker than those of adjacent cells.[70] Presumably, this could explain why they always appear as dark bands in reflectance images of the nerve fiber layer. Müller cells have greater cytoplasmic densities than the neurons in their microenvironment and mitochondrial organelles are distributed all across the cell body within Müller cells, from the inner to the outer retina.[70] We speculate that a combination of greater cytoplasmic density coupled with mitochondrial distribution could enhance two-photon excited fluorescence within Müller cells, thus making them brighter than the nerve fiber bundles. Fluorophores, such as NAD(P)H, could be the source of this enhanced autofluorescence.

Two-Photon Autofluorescence From Vessel Walls

Vessel walls also were autofluorescent upon 730 nm two-photon excitation. The strength of the autofluorescent signal was related to the size and thickness of the vessel. Fluorescence from relatively larger, thicker primary vessels close to the optic disk was greater than that from smaller vessels further away from the disk, although faint fluorescence still was visible from smaller vessels. Fluorescence from vessel walls varied with the focus and a through-focus image stack is shown in the right column of Figure 3. Corresponding reflectance images also are shown for comparison in the left column and were collected with a different light source than that used for fluorescence. Alignment and cofocusing errors between these two light sources hindered an exact alignment of spatial features between these fluorescence and reflectance images. For relatively vitreal focus depths, fluorescence was detected from cross-sections of the vessel walls as well as en face fluorescence from the vessels (Figs. 3b, 3d). At these focal planes, Müller cell processes were visible adjacent to the vessels. Unlike the fluorescence images, the vessel walls were not always clearly defined in the reflectance images (Figs. 3a, 3c). At deeper focal planes when the beam was focused within a vessel, two bright streaks of approximately 15 μm mean thickness were visible due to strong autofluorescence from a cross-section of the vessel walls (Fig. 3f). When the vessel was above the plane of focus as in Figure 3h, it prevented light from reaching the layers below it, thus casting a dark shadow.

Vessel walls are composed of three layers: the adventitia, media, and lumen. The source of diffuse fluorescence from vessel walls is likely due to proteins, such as collagen in the adventitia and elastin in the media.[49,73–77] Collagen is autofluorescent but, based on previous studies on two-photon microscopic imaging of arteries, elastin is likely the dominant fluorophore upon $\lambda_{ex} = 730$ nm excitation.[74]

In some cases, bright granular structures were present close to the vessel walls of some of the larger vessels near the optic disk (Fig. 4). These granular features were observed within vessel walls in two of the animals imaged in this study. In one of the subjects, at locations away from the optic disk, relatively bright autofluorescence could be seen from rotund structures outside the walls of smaller vessels, but always adjacent to them. However, there was variability between animals and these features were not always visible near every vessel. The source of this fluorescence from bright structures within and near vessel walls, as shown in Figure 4, is unknown, but there are several possibilities.

1. Different types of glial cells, such as astrocytes and pericytes, are always adjacent to blood vessels.[70] As shown in Figure 2, Müller glial cells exhibit greater two-photon autofluorescence and yield positive contrast compared to adjacent tissue cells. Similarly, other glial cells conceivably could yield greater autofluorescence than their surroundings.
2. Vessel walls contain other possible sources of autofluorescence as well. Advanced glycation end-products (AGEs) form as a result of glycation of proteins present within vessels. This is a natural process that happens with age, and can be accelerated by disease.[78] These AGEs also are known to be fluorescent and the increase in fluorescence with glycation is greater for collagen than for elastin.[79]
3. Animals used in these studies were subjected to fluorescein on multiple occasions. It also is possible that the bright structures seen within and without vessel walls could be due to clusters of particulates of the exogenous dye that leaked out of blood circulation, although the likelihood of fluorescein leakage is low.

Two-photon imaging could be used to study the biomechanics and rheologic integrity of blood vessels in the living eye because fluorescence from collagen and elastin proteins is a natural biomarker for vessel strength. Thus, it would be

Investigative Ophthalmology & Visual Science

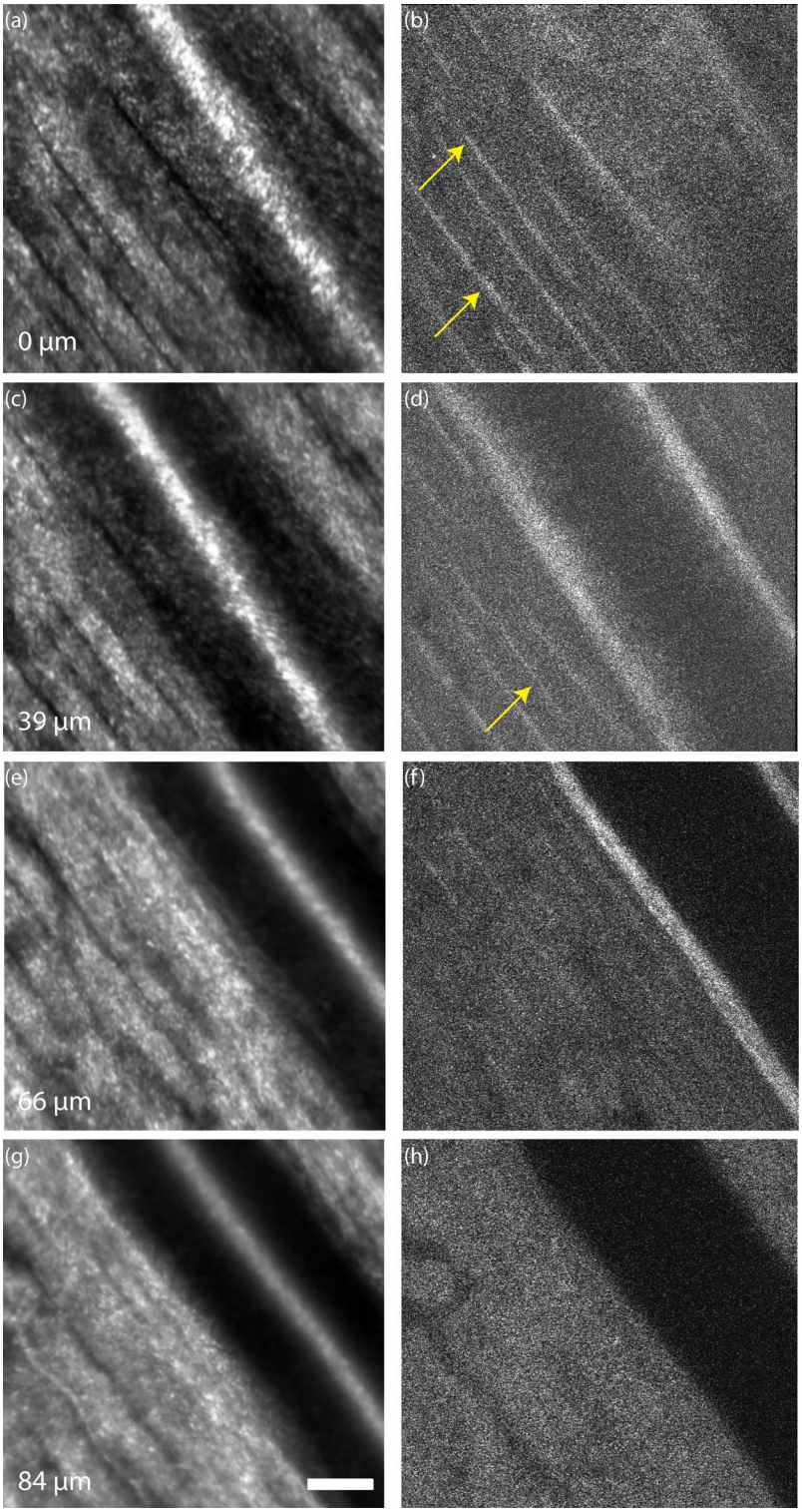

Figure 3. Through-focus image stack of a blood vessel in the retina is shown here. Reflectance images are shown in the left in (**a**), (**c**), (**e**), and (**g**), with (**a**) being the most vitreal and (**g**) the most scleral. The corresponding two-photon images at 730 nm excitation are shown on the right, (**b**), (**d**), (**f**), and (**h**). In (**b**), edges of the vessel walls were almost indistinguishable and the two-photon fluorescence signal from the en face vessel walls was dominant. Müller cell processes are visible in (**b**) and (**d**) and are indicated with *yellow arrows*. At a focus location (**d**), the vessel walls were visible, but the relative contrast with respect to the fluorescence within the vessel was lower than in (**f**) where the vessel boundaries were strongly fluorescent. The characteristic *dark shadow* of the vessel is visible in (**h**). Two-photon imaging conditions: power at the cornea, 7 mW; scan size, 1.1° × 1.3°; duration of recording, 9600 frames (436 seconds); exposure, 3617 J/cm^2. Exposure was greater than MPE by a factor of 8. *Scale bars*: 50 µm.

Investigative Ophthalmology & Visual Science

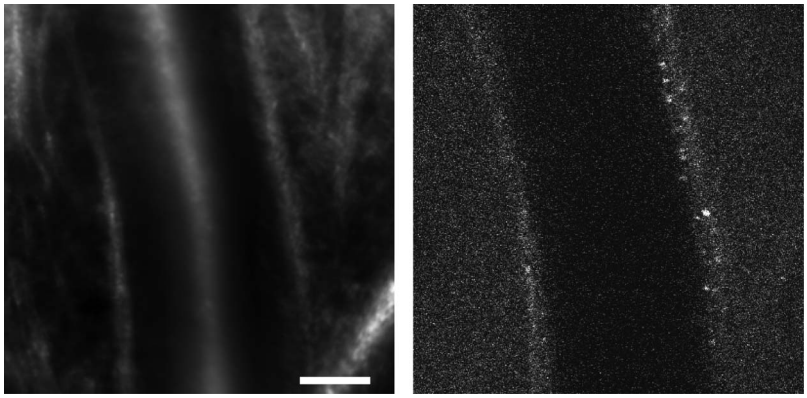

FIGURE 4. (**a**) Reflectance image of an artery close to the optic disk, and (**b**) the corresponding two-photon fluorescence image collected at the same location. Fluorescence from bright granular structures can be seen within the vessel wall in (**b**). Two-photon imaging conditions: power at the cornea, 7 mW; scan size, 1.5° × 1.54°; duration of recording, 19,200 frames (873 seconds); exposure, 4598 J/cm². Exposure was greater than MPE by a factor of 8.6. *Scale bars*: 50 μm.

interesting to characterize autofluorescence from vessels under conditions of stress, such as hypertension, diabetic retinopathy, infarction, and so forth. The potential to image AGEs also could be used to study aggregation of these harmful products on vessel walls during aging and disease.

Two-Photon Autofluorescence From the Inner Retina

At layers more scleral than the nerve fiber layer, structural features seen in two-photon autofluorescence images differed from those seen in reflectance imaging. Close to the nerve fiber layer, autofluorescence from a mosaic of dark, elliptical-shaped features was noted. The distribution and density of these dark spots were not uniform and changed with the focus of the imaging beam. At some locations, these dark disks were visible within the entire volume as far as 20 to 30 μm below the best focus for Müller cell processes in the nerve fiber bundles. We hypothesize that these dark disks could be nuclei of cells in the ganglion cell layer. Although the outlines of all cells could not be identified reliably, nuclei of some cells were more clearly visible than others. The size of these circular features were approximately 5 to 15 μm, within the same range as values reported by Curcio and Allen.[80] For a subset of imaged locations, in vivo data were compared with ex vivo histologic data captured by two-photon microscopy of the ganglion cell layer from the same retinal location. The radial average of the Fourier transforms for in vivo and ex vivo images peaked at similar spatial frequencies as shown in Figure 5, suggesting that the density of cells in the in vivo images is consistent with their histology.

In vivo through-focus images from a location that was 16° temporal and inferior to the fovea are shown in Figure 6. The column on the left shows the reflectance images, while the column on the right displays the corresponding autofluorescence images collected at the same location from the same light source but at different focal planes. Rows of spot-like features arranged linearly, like strings of pearls, oriented along the nerve fiber bundles that lie just above them could be visualized (Fig. 6b). This distribution is similar to ex vivo images of ganglion cells captured by phase microscopy.[81] Near large vessels, the distribution of these cells was heterogeneous across the field at different focal planes with a band of cells visible closer to the vessel at shallow focal planes and seemingly located further away from the vessel at relatively deeper focal planes. This distortion in the ganglion cell layer near large vessels also was observed in ex vivo two-photon images (data not shown).

At focal planes that were approximately 40 μm more scleral than the image shown in Figure 6b, string of pearl-like features were still visible. Images from these focal planes are shown in Figure 6d. At focal planes that were approximately 10 μm more scleral, we did not observe any mosaic-like features although

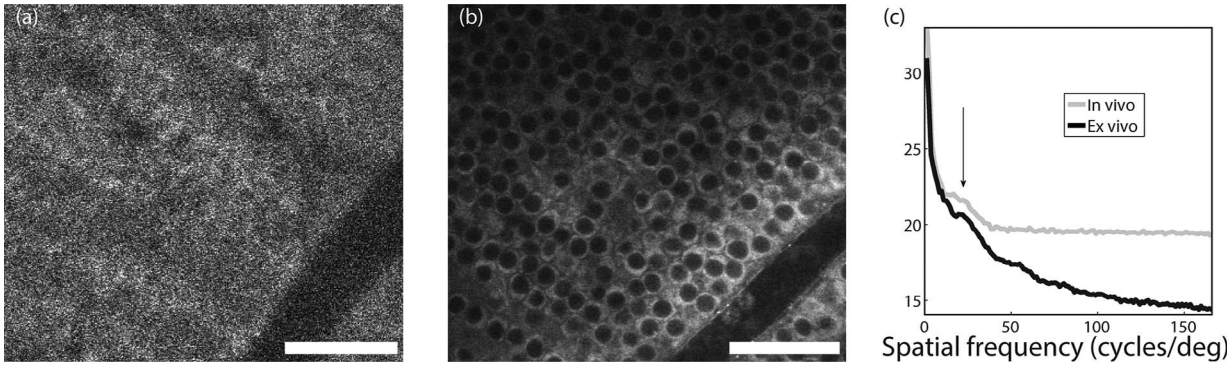

FIGURE 5. Comparison of in vivo and ex vivo two-photon autofluorescence, $\lambda_{ex} = 730$ nm from the same retinal location, 8° nasal to the fovea. (**a**) Two-photon image of the living eye. (**b**) Two-photon image of fixed tissue from the same eye at the same location. (**c**) Radial average of the Fourier transform for both images plotted on the same scale. The peak corresponds to a cell spacing ranging from 10 to 18 μm. In vivo two-photon imaging conditions: power at the cornea, 7 mW; scan size, 1.1° × 1.3°; duration of recording, 12,800 frames (582 seconds); exposure, 4823 J/cm². Exposure was greater than MPE by a factor of 8.5. *Scale bars*: 50 μm.

Investigative Ophthalmology & Visual Science

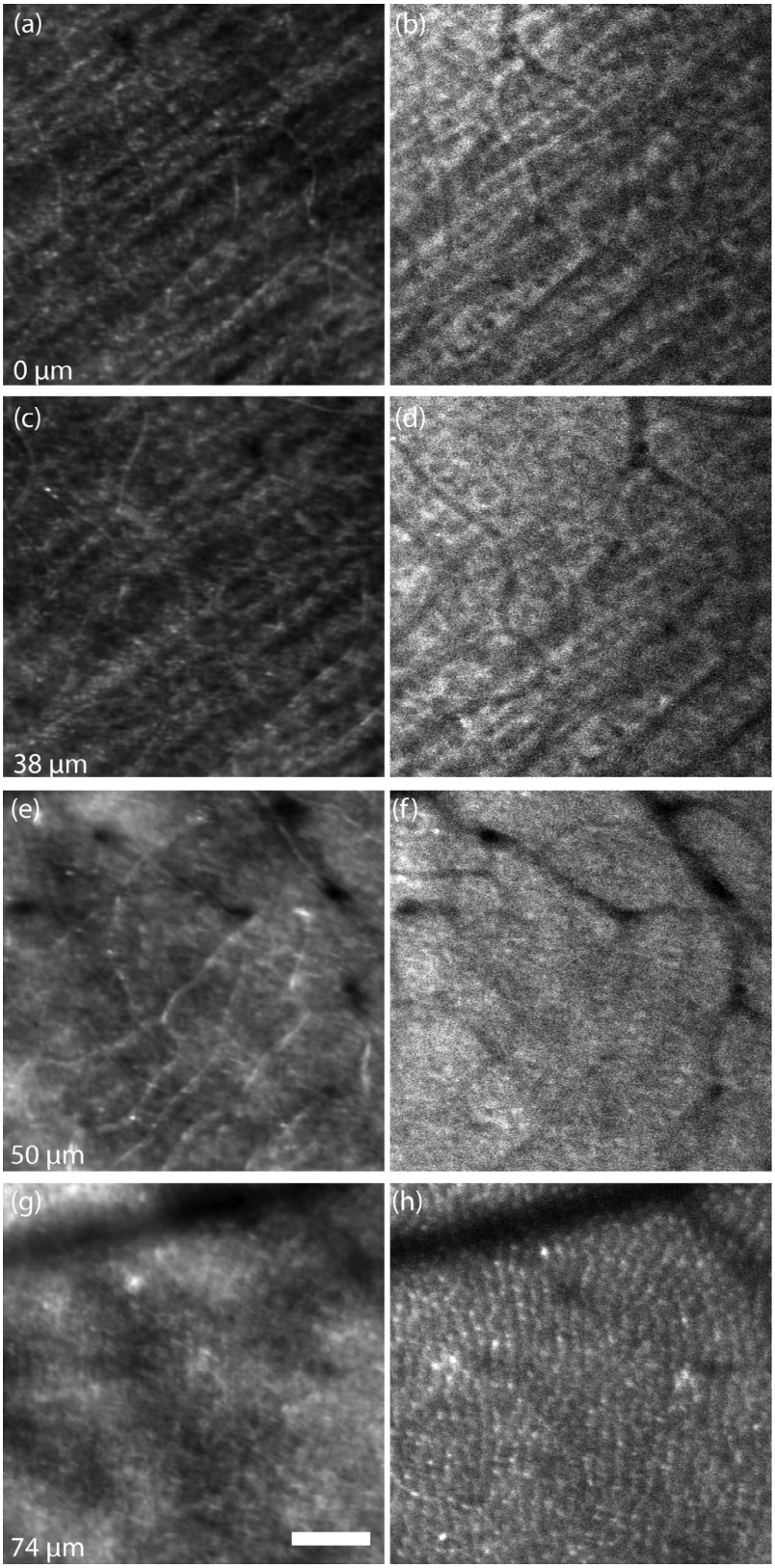

FIGURE 6. Through-focus images of the inner retina acquired at $\lambda_{ex} = 730$ nm. Reflectance images are shown in the *left column* and autofluorescence images from the same location are shown in the *right column*. Nerve fiber bundles imaged using a conventional confocal reflectance modality are shown in (**a**) and (**c**) while ganglion cell nuclei can be seen arranged along the nerve fiber bundles in (**b**) and (**d**). A reflectance image from a capillary bed in the inner retina is shown in (**e**) while autofluorescence from the same location (**f**) reveals a distinct lack of structural contrast compared to (**b**) and (**d**). At a more scleral focal plane, a reflectance image is shown in (**g**), and the corresponding autofluorescence image is shown in (**h**). In (**b**), (**d**), and (**h**) a mosaic of cells is visually distinguishable in autofluorescence but not in reflectance images. Relative axial separation between the different axial slices is noted on the *bottom left* in the *left column*. Two-photon imaging conditions: power at the cornea, 14 mW; scan size, $1.1^\circ \times 1.3^\circ$; duration of recording, 16,200 frames, forward and back scan combined (395 seconds); exposure, 6551 J/cm^2. Exposure was greater than MPE by a factor of 15.4. *Scale bars*: 50 µm.

Investigative Ophthalmology & Visual Science

capillaries still remained visible (see Figs. 6e, 6f). The presence of capillaries and their relative separation from the ganglion cell layers suggests that this locus is likely to be in the vicinity of the inner plexiform layer.[81] Images from a deeper focal plane, expected to be the outer nuclear layer, are shown in Figures 6g and 6h. A mosaic of dark, circular cell-like structures, separated from each other by relatively bright boundaries was visually distinguishable in the fluorescence image. Sparsely distributed bright punctate spots also were visible along the cell boundaries. The radial average of the Fourier transform of the fluorescence image peaked at spatial frequencies corresponding to an average cell-to-cell spacing of approximately 13 μm.

Two-photon microscopy has previously revealed that fluorescence in nuclear layers is greater from structures outside cells than from within them.[56,57] This results in negative cellular contrast, presumably due to diminished fluorescence from within the nuclei or cytoplasm of individual cells. While the source of autofluorescent contrast is debatable, there are several likely explanations.

1. Spectroscopy has shown that the primary sources of fluorescence in the inner retina are metabolic functional indicators, such as FAD and NAD(P)H.[82,83] These mitochondrial molecules are key participants in the electron transport chain and citric acid cycle. Sparse quantities of mitochondria are present throughout the inner retina as revealed by cytochrome oxidase labeling of primate retina.[84] Studies on brain slices have shown that these molecules have an important role during synaptic activation[50,85,86] and likely could contribute to autofluorescence from various layers in the inner retina.[87]
2. Müller cells reportedly are the dominant source of autofluorescence in the inner retina of frogs[55] and we have shown that fluorescence from Müller cell processes is greater than from nerve fiber bundles. Although the molecules responsible for relatively greater autofluorescence from Müller cells are debatable and unconfirmed, these glial cells span the entire depth of the retina, from the inner to the outer limiting membrane. In the inner retina, Müller cells wrap around the cell bodies of retinal neurons[70] and due to their distribution with respect to secondary and tertiary neurons in the retina they possibly could be responsible for the inherent cellular contrast in the nuclear layers.
3. Autofluorescence from the extracellular matrix also could potentially contribute to the intrinsic contrast of nuclear layers upon two-photon excitation at 730 nm. The extracellular matrix that supports these neurons is composed of a variety of proteins such as collagen, elastin, laminin, fibronectin and others that are all autofluorescent to various degrees.[88,89]

Two-Photon Autofluorescence From Outer Retinal Layers

With 730 nm excitation, through-focus images of the outer retina were collected at multiple focal planes. Fluorescence from the cone photoreceptor mosaic was visible at all focal planes but individual rods could be resolved only at a single focal plane and their fluorescence was dimmer than that of cones (see Fig. 7h). At some focal planes that were more vitreal than the best focus for rods, dark, granulated sub-cellular structures were observed within the cell outlines of cone photoreceptors. These bullseye-like features were not always located at the center of each cone, but were present somewhere within the outline of some cells (see Figs. 7c, 7f). These features were not visible at the focal plane for best focus of rods (Fig. 7i), or at deeper focal planes (Fig. 7l). In appearance, they resembled images of cone inner segments labeled with cytochrome oxidase,[84] suggesting that molecules, such as NAD(P)H and FAD, present within mitochondria could account for the fluorescence from inner segments.

Alternatively, the bullseye like features also could be due to higher order waveguiding modes in cones that also are seen in the reflectance images.[90,91] This would suggest a very strong correlation between waveguiding and two-photon autofluorescence that requires further investigation. At deeper focal planes, fluorescence from out-of-focus cones could be visibly distinguished (see Figs. 7k, 7l). The RPE mosaic was not visible even at the most scleral focal planes that we imaged, though in vivo and ex vivo studies have shown that RPE cells also are autofluorescent upon 730 nm excitation.[56,92,93]

Two-Photon Excited Autofluorescence From RPE Cells and Photoreceptors

As shown in Figure 1, autofluorescence upon 920 nm excitation was primarily from the outer retina. In the excitation wavelength range of 900 to 920 nm, cellular structures were observed at multiple focal planes. The size, density, and distribution of these cellular features changed with the eccentricity and plane of focus. At a location 4° nasal to the fovea, reflectance and fluorescence images collected at several focal planes are presented in Figure 8. At all focal planes, reflectance images (left column) show the characteristic distribution of cones, whereas rods are easier to visualize in some planes than others, such as in Figures 8d and 8g. This also is evident from the radial averages of the Fourier transforms (right column) which peaked at the spatial frequencies corresponding to the cone mosaic. For most through-focus positions, outlines of cellular structures were visible in fluorescence images as well. These structures were characteristically larger than cones and could be seen at multiple focal planes, even when out of focus (Figs. 8b, 8e, 8h, 8k). Radial averages of the Fourier transform of fluorescence images peaked at spatial frequencies lower than the cone mosaic and are likely indicative of the RPE cell mosaic. For these data, the peak spatial frequency corresponded to an average density of 3100 cells/mm^2 with an average nearest neighbor distance of approximately 19 μm. This packing is less dense than the average values reported previously in macaques at these eccentricities (4500 cells/mm^2 and 13.1 μm) by Morgan et al.[94] At some focal planes, finer structures could be seen within the outlines of RPE cells. For instance, at a focal plane where cones and some rods were visible in reflectance images (Fig. 8g), granular features could be seen in fluorescence images within RPE cells that were similar in size and distribution to those in photoreceptors (Fig. 8h). Some cells that could be seen in reflectance also were visible in fluorescence images, as indicated by arrows pointing to cones (in yellow) and rods (in red). Accordingly, the location of each photoreceptor could be identified with respect to the RPE cell underneath.

The appearance of fluorescent cellular features varied with retinal eccentricity as well. We recorded autofluorescence with 900 nm excitation at several eccentricities along the temporal meridian at focal planes where the cone photoreceptors were in focus in reflectance. Two such cases are shown in Figure 9 at locations that were 1.6° and 7.7° temporal to the fovea. The typical distribution of cone photoreceptors could be seen in reflectance images at both eccentricities (Figs. 9a, 9d). In the fluorescence image recorded at the location closer to the fovea (Fig. 9b), small cellular features, arranged in a tightly packed mosaic, were seen. These structures were of the same spatial

Investigative Ophthalmology & Visual Science

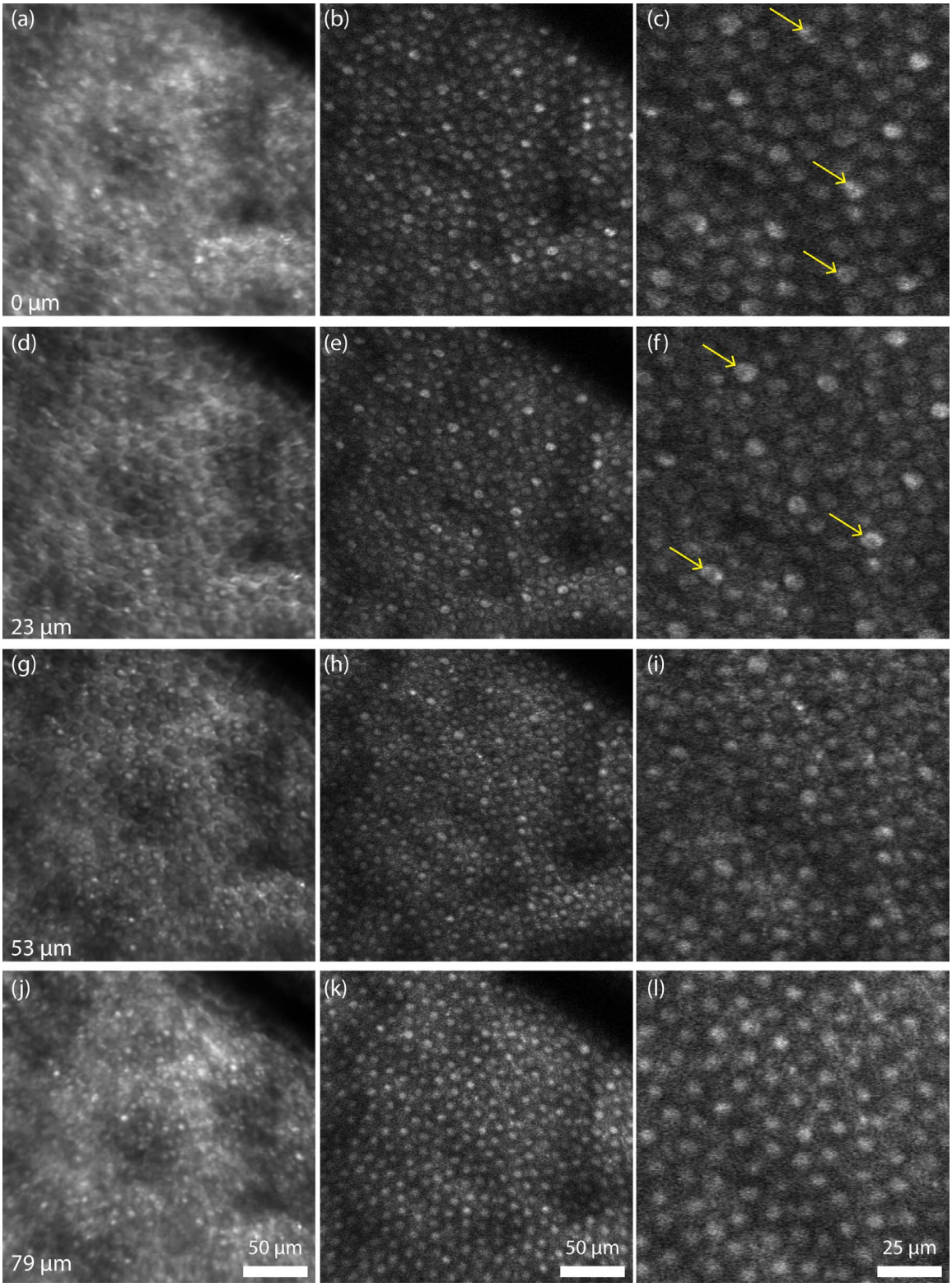

Figure 7. Through-focus images of the outer retina at $\lambda_{ex} = 730$ nm. Reflectance images are shown in the *left column* and autofluorescence images captured from the same location are shown in the *middle column*. Zoomed-in autofluorescence images are shown in the *right column*. Dimples in the cross-section of fluorescence from some cones can be seen in (**c**) and (**f**). The best focus for rods is shown in (**h**) and (**i**) while out of focus photoreceptors can be seen in deeper focal planes as revealed in (**k**) and (**l**). Relative axial separation between the different optical slices is noted on the *bottom left* in the *left column. Yellow arrows* point to cells where bulls-eye features are clearly visible. Two-photon imaging conditions: power at the cornea, 7 mW; scan size, $1.1° \times 1.3°$; duration of recording, 10,800 frames, forward and back scan combined (263 seconds); exposure, 2184 J/cm^2. Exposure was greater than MPE by a factor of 7. *Scale bars*: 50 µm.

Investigative Ophthalmology & Visual Science

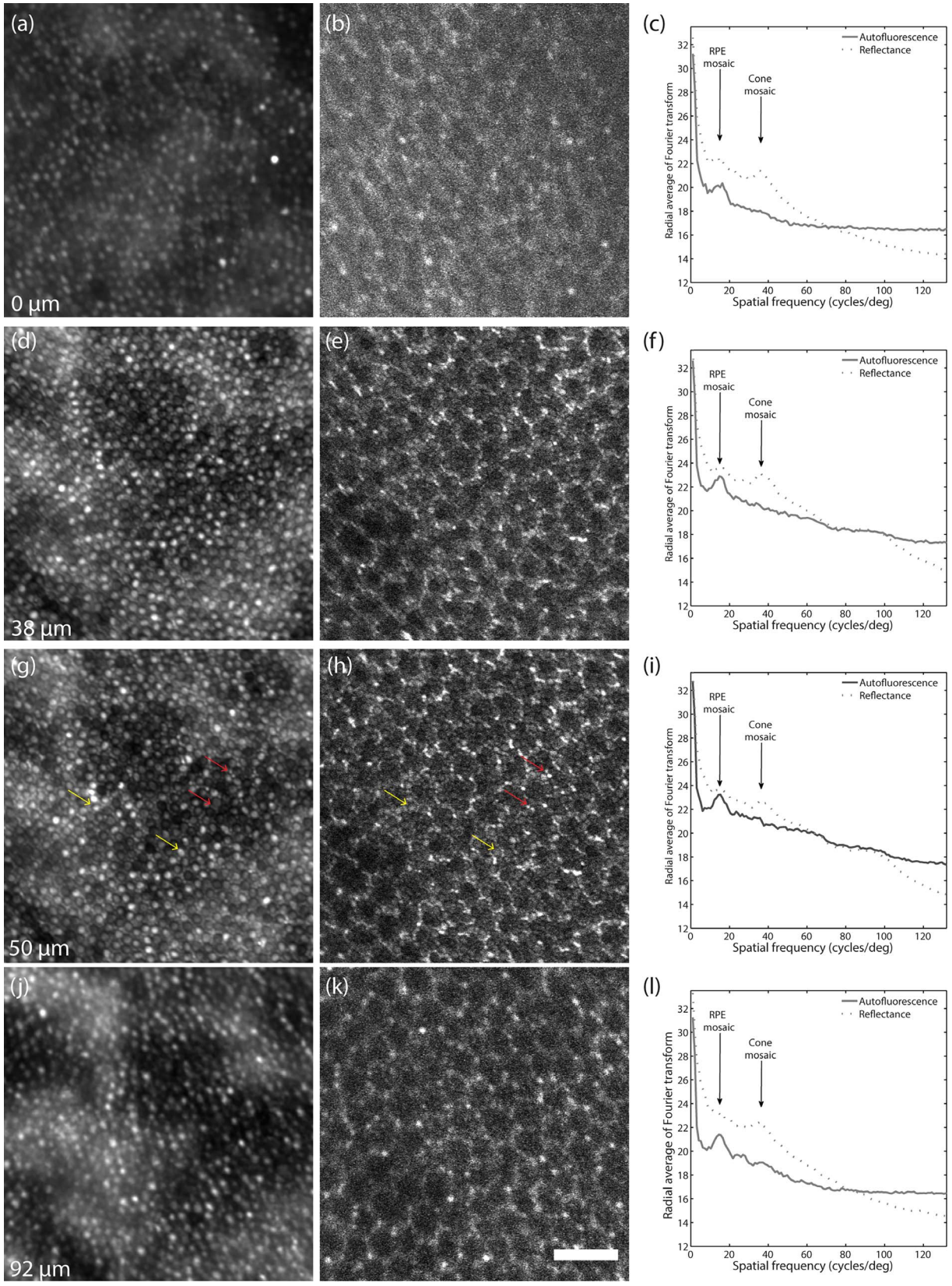

Figure 8. Through-focus images of the outer retina at $\lambda_{ex} = 920$ nm at a location that was 4° nasal to the fovea. Reflectance images are shown in the *left column* and autofluorescence images from the same location are featured in the *center column*. Radial averages of the Fourier transforms are shown in the *right column*. Outlines of RPE cells are visible in all fluorescence images and photoreceptors are visible in all reflectance images and in some fluorescence images as also can be noted in the Fourier transforms. *Yellow arrows* point to the same cones and *red arrows* to same rods in (**g**) and (**h**). Radial averages of the Fourier transforms for (**g**) and (**h**) show that the rod and cone mosaic can be seen in the fluorescence image. Two-photon imaging conditions: power at the cornea, 7 mW; scan size, 1.1° × 1.3°; duration of recording, 21,600 frames, forward and back scan combined (527 seconds); exposure, 4367 J/cm^2. Exposure was greater than MPE by a factor of 3.5. *Scale bars*: 50 µm.

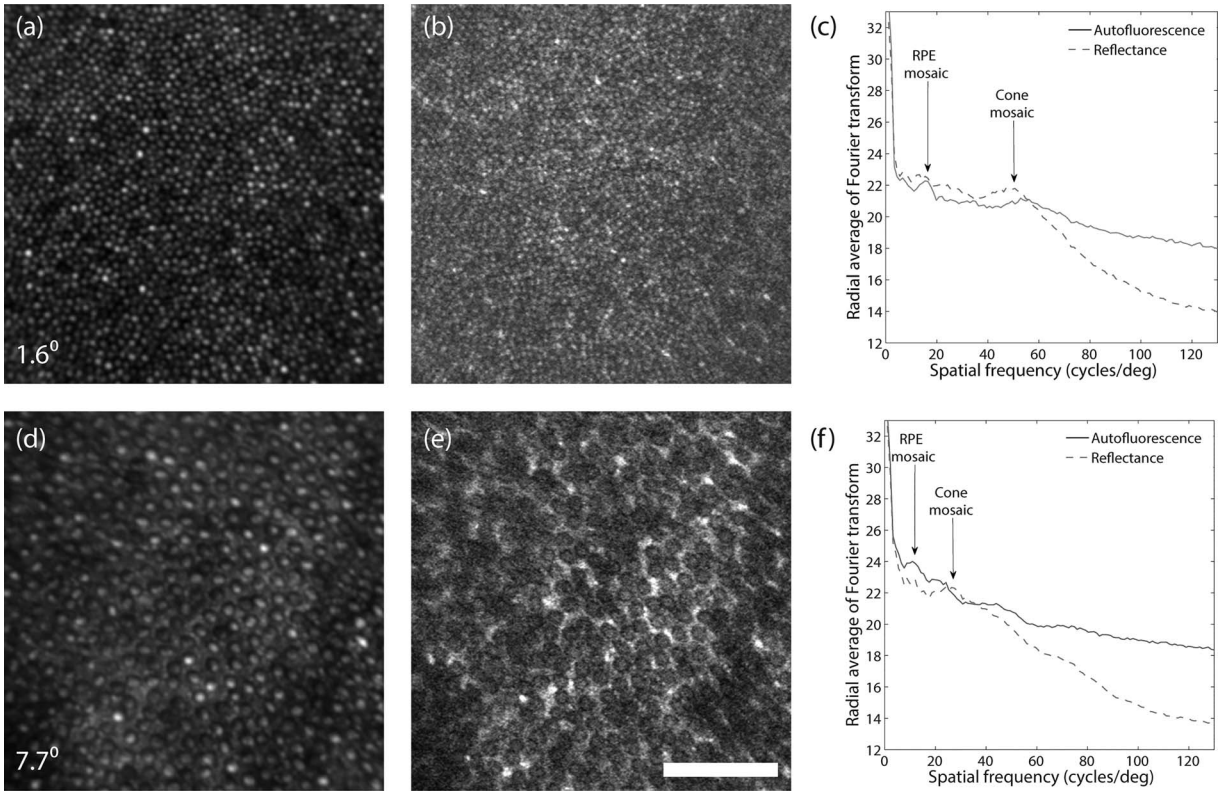

Figure 9. Images at $\lambda_{ex} = 900$ nm from two different retinal locations in the same subject. Images in (**a**) (**b**) are from a location that was 1.625° temporal to the fovea, whereas images in (**e**) and (**f**) were recorded at 7.7° temporal to the fovea. Both (**a**) and (**d**) are reflectance images of the photoreceptor mosaic, whereas (**b**) and (**e**) are two-photon autofluorescence images from the corresponding locations. *Graphs* shown in (**c**) and (**f**) are radial averages of the Fourier transforms for the images shown in (**a**) and (**b**), and (**e**) and (**f**) respectively. Two-photon imaging conditions: power at the cornea, 2.6 mW; scan size, 1.1° × 1.3°; duration of recording, 3200 frames (145 seconds); exposure, 448 J/cm^2. Exposure was greater than MPE by a factor of 1.02. *Scale bars*: 50 μm.

scale as photoreceptors visible in the corresponding reflectance image in Figure 9a. The radial average of the Fourier transform (shown in Figure 9c) peaked at two different frequencies, corresponding to the mosaic of photoreceptors, as well as underlying RPE cells at this location. The fluorescence image recorded further away from the fovea looked distinctly different. At this and other locations away from the fovea, a sparse mosaic of relatively dim, circular cell-like structures could be distinguished (Fig. 9e). The size and density of dim cells seen in fluorescence was identical to the size and distribution of cone photoreceptors visible in reflectance (Fig. 9d), thus strongly suggesting that these dim cells are cones. Although autofluorescence could be visualized within these cells, most cones appeared darker than the surrounding cells which we know to be rods. This implies that at these retinal eccentricities and focal planes, fluorescence from rods is brighter than cones as well as RPE cells.

To our knowledge, pattern masking of RPE autofluorescence by the overlying photoreceptor mosaic has not been reported with in vivo single-photon excitation imaging of the outer retina at wavelengths >500 nm.[19] However, our data suggest that two-photon imaging with 900 to 920 nm can excite fluorescence from RPE cells, as well as from cone and rod photoreceptors and that the pattern is dependent on focus and eccentricity. At these excitation wavelengths, lipofuscin and its precursors are likely to be the dominant source of autofluorescence in RPE cells.[45] Moreover, fluorescence from lipofuscin precursors, such as A2E, also has been detected in rod outer segments in isolated cells.[95] We hypothesized that A2E and/or other lipofuscin precursors could be responsible for the observed fluorescence from the outer retinal cells upon 900 to 920 nm excitation. Additionally, rhodopsin also is known to be autofluorescent[96] and its contribution could explain why the fluorescence from rods was greater than from cones and RPE cells in Figure 9e. However, the fluorescence efficiency of A2E is approximately 2 orders of magnitude greater than that of rhodopsin.[97] Another possible explanation for the appearance of photoreceptor mosaic interleaved with the RPE mosaic could be due to concentration of light at the outer segment tips due to waveguiding by photoreceptors but this hypothesis has not been verified.

Conclusions

From the time of Helmholtz to today, many significant advances have been made in our ability to image the retina and in vivo two-photon ophthalmoscopy adds to the list of retinal features that can now be visualized at a cellular level. Naturally occurring endogenous fluorophores in the retina provided the intrinsic optical contrast needed to visualize many structural features that have never been reported before in the living primate eye. Examples include Müller cell processes in the inner retina, outlines of ganglion cells and photoreceptor nuclei, bulls-eye like features within photoreceptor segments and the arrangement of photoreceptors relative to their neighboring RPE cells. Light levels used for imaging the structures reported here were higher than the maximum permissible exposure (MPE) dictated by ANSI,[98] ranging from a factor of 1.02 (Fig. 9) to a factor of 15 (Fig. 6) greater than the MPE. In many cases, images were collected at light levels and

Investigative Ophthalmology & Visual Science

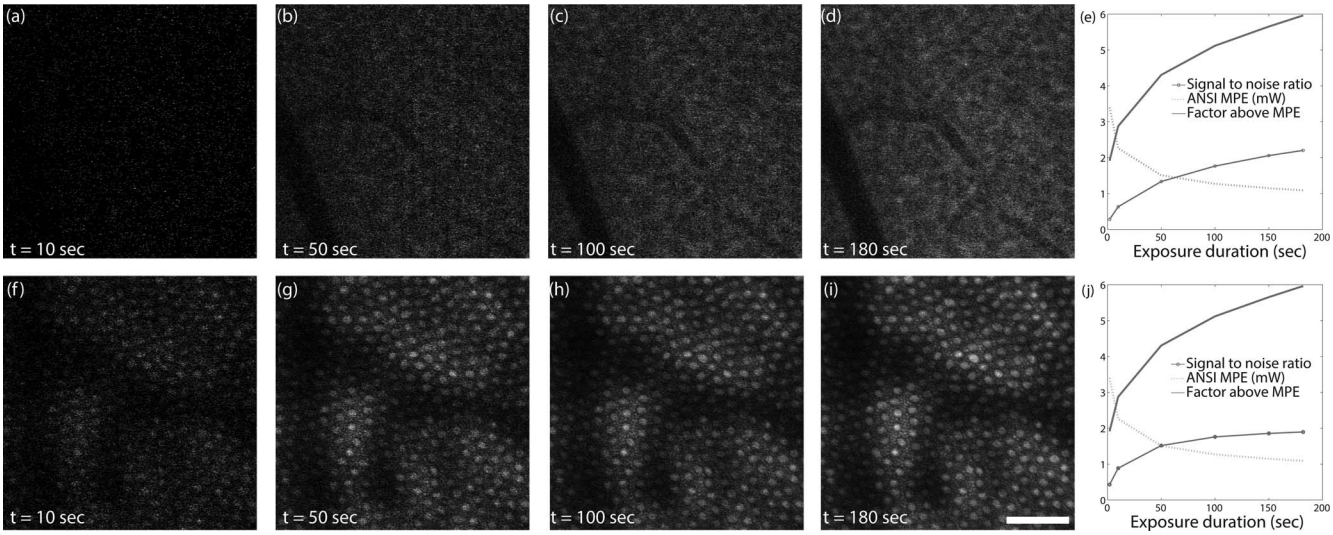

Figure 10. Images at $\lambda_{ex} = 730$ nm from a retinal location 15° temporal to the fovea. Data shown in the *top row* were collected at the ganglion cell layer, while data in the *bottom panel* are from the photoreceptor layer. Images shown in different *columns* were generated after integrating data collected over different periods of exposure duration, ranging from 10 seconds in (**a**) and (**f**), 50 seconds in (**b**) and (**g**), 100 seconds in (**c**) and (**h**), and 180 seconds in (**d**) and (**i**). Plots shown in (**e**) and (**j**) show the evolution of the signal-to-noise ratio measured from these images as a function of exposure duration, as well as the maximum permissible exposure dictated by ANSI in mW. Two-photon imaging conditions were as follows: power at the cornea, 6.5 mW; scan size, 1.1° × 1.3°; duration of recording, 4000 frames (0–180 seconds); exposure, 1400 J/cm^2. The ratio of light level to allowed MPE is plotted in (**e**) and (**j**) for different exposure durations.

exposure durations greater than what were required to visualize many relevant structural details; but as expected, the quality of the images and the signal-to-noise ratio improved with higher exposure durations (Fig. 10). Although we did not observe obvious signs of damage to these retinal locations for the data reported here, a more detailed study currently is in progress to carefully assess the damage threshold for in vivo two-photon imaging. All the same, improvements in light delivery, signal detection and other technical advances are needed to make two-photon autofluorescence imaging of the retina safe for use in human subjects.

In vivo two-photon imaging provides a novel modality for studying Müller cell processes. These cells perform a variety of roles in the inner and outer retina, especially in regulating axonal current and ionic channels in the nerve fiber layer.[99,100] The ability to image Müller cells intertwined with nerve fiber bundles offers the possibility of investigating their behavior in pathologies, such as macular telangiectasia,[101] glaucoma, idiopathic intracranial hypertension, papilledema, and other diseases involving the nerve fiber layer.

Autofluorescence from vessel walls is likely due to proteins, such as collagen and elastin, which are natural biomarkers for vessel strength. Two-photon imaging could be used to study the biomechanics and rheologic integrity of blood vessels in the living eye, especially under conditions of stress, such as hypertension, diabetic retinopathy, infarction, and so forth. Such imaging also could be used to track the progression of AGEs with age and disease.

Fluorescence from the ganglion cell layer as well as outer nuclear layer is well documented.[56,57] Ganglion cells are severely compromised in diseases, such as glaucoma, and there could be great value in imaging the ganglion cell layer and potentially counting these cells in normal and diseased living eyes. With improvements in two-photon imaging, this technology could enable clinicians to track the progression of retinal diseases in patients over time. Additionally, since metabolites, such as NAD(P)H and FAD, are likely to be the source of fluorescence, two-photon imaging could be used to probe the functional activity of these cells without extrinsic labeling.

Autofluorescence from photoreceptors has been reported previously in ex vivo and in vivo studies. Here, we report images of subcellular features within cone photoreceptors. While the in vivo images shown here are inconclusive, we speculate that these could be related to the distribution of mitochondria within the inner segments.[84] This is of scientific and clinical interest since it is known that mitochondrial distribution changes in diseases, such as age-related macular degeneration.[102] Previous studies have focused on time-dependent changes in fluorescence from photoreceptors[60,103] and suggest that retinoids in the outer retina are likely responsible for time-variable autofluorescence. The ability to track the visual cycle could enable investigations of diseases, such as retinitis pigmentosa and others,[51] that affect photopigment regeneration.

At 900 to 920 nm excitation wavelengths, we observed autofluorescence from photoreceptors as well as RPE cells, possibly due to lipofuscin precursors. This could be used to monitor lipofuscin generation mechanisms in the living eye. Although single-photon imaging of the RPE mosaic can now be accomplished at safe light levels, the visible wavelengths used for imaging are bright and can be uncomfortable for human subjects. Two-photon imaging provides an alternative way to image the RPE mosaic with less-intrusive infrared light at 920 nm and potentially could be used for clinical imaging.

In conclusion, the observations reported here demonstrated the value of in vivo two-photon retinal imaging. The presence and distribution of various endogenous fluorophores have enabled visualization of a variety of structures in the retina. Although the identities of the dominant sources of fluorescence from different retinal layers still are not fully understood, there is no shortage of potential scientific and clinical applications. With further improvements, this technique could be made safer and eventually be used for noninvasive imaging of all cellular layers, thus providing a whole new way to visualize changes in retinal structures in normal and diseased eyes.

Investigative Ophthalmology & Visual Science

Acknowledgments

The image acquisition software and firmware were developed by Qiang Yang, adaptive optics control software by Alfredo Dubra and Kamran Ahmad, image registration software by Alfredo Dubra and Zachary Harvey. The stereotaxic cart design was a courtesy of the United States Air Force, and the cart was constructed by Martin Gira and Mark Ditz. Animals were handled by Lee Anne Schery, Tracy Bubel, Amber Walker, or Louis DiVincenti before and during experimentation. The authors thank Christina Schwarz, Keith Parkins, Ethan Rossi, Jesse Schallek, Jie Zhang, Benjamin Masella, and Ted Tweitmeyer for their contributions.

Supported by the National Eye Institute and the National Institute of Aging of the National Institutes of Health under Award Numbers R44 AG043645, R01 EY022371, R24 EY024864 and P30 EY001319, BRP-EY014375 and K23-EY016700. The content is solely the responsibility of the authors and does not necessarily represent the official views of the National Institutes of Health. This study was also supported by an unrestricted grant to the University of Rochester Department of Ophthalmology from Research to Prevent Blindness, New York, New York and by grants from the Arnold and Mabel Beckman Foundation. K.P. is John H. Hord Professor of Pharmacology.

Disclosure: **R. Sharma**, Polgenix, Inc. (F), P; **D.R. Williams**, Polgenix, Inc. (F), Canon (F), P; **G. Palczewska**, Polgenix, Inc. (E); **K. Palczewski**, Polgenix, Inc. (C), P; **J.J. Hunter**, Polgenix, Inc. (F), P

References

1. Helmholtz H. *Beschreibung Eines Augen-Spiegels*. Berlin, Heidelberg: Springer Berlin Heidelberg; 1851.
2. Jackman W, Webster J. On photographing the eye of the living human retina. *Phila Photogr*. 1886;23:340–341.
3. Howe L. Photography of the Interior of the Eye. *Trans Am Ophthalmol Soc*. 1887;4:568–571.
4. Dimmer F, Pillat A. *Atlas photographischer Bilder des menschlichen Augenhintergrundes*. Leipzig, Wien, Germany: F. Deutickel; 1927.
5. Novotny HR, Alvis DL. A method of photographing fluorescence in circulating blood in the human retina. *Circulation*. 1961;24:82–86.
6. Webb RH, Hughes GW, Pomerantzeff O. Flying spot TV ophthalmoscope. *Appl Opt*. 1980;19:2991.
7. Webb RH, Hughes GW. Scanning laser ophthalmoscope. *IEEE Trans Biomed Eng*. 1981;28:488–492.
8. Fercher AF, Roth E. Ophthalmic laser interferometry. *Proc SPIE*. 1986;0658:48–51.
9. Huang D, Swanson E, Lin C, et al. Optical coherence tomography. *Science*. 1991;254:1178–1181.
10. Swanson EA, Izatt JA, Hee MR, et al. In vivo retinal imaging by optical coherence tomography. *Opt Lett*. 1993;18:1864–1866.
11. Fercher AF, Hitzenberger CK, Drexler W, Kamp G, Sattmann H. In vivo optical coherence tomography. *Am J Ophthalmol*. 1993;116:113–114.
12. Hee MR, Izatt JA, Swanson EA, et al. Optical coherence tomography of the human retina. *Arch Ophthalmol*. 1995;113:325–332.
13. Drexler W, Morgner U, Ghanta RK, Kärtner FX, Schuman JS, Fujimoto JG. Ultrahigh-resolution ophthalmic optical coherence tomography. *Nat Med*. 2001;7:502–507.
14. Liang J, Williams DR, Miller DT. Supernormal vision and high-resolution retinal imaging through adaptive optics. *J Opt Soc Am A*. 1997;14:2884–2892.
15. Roorda A, Romero-Borja F, Donnelly I, Queener H, Hebert T, Campbell M. Adaptive optics scanning laser ophthalmoscopy. *Opt Express*. 2002;10:405–412.
16. Zhang Y, Rha J, Jonnal R, Miller D. Adaptive optics parallel spectral domain optical coherence tomography for imaging the living retina. *Opt Express*. 2005;13:4792–4811.
17. Dubra A, Sulai Y, Norris JL, et al. Noninvasive imaging of the human rod photoreceptor mosaic using a confocal adaptive optics scanning ophthalmoscope. *Biomed Opt Express*. 2011;2:1864–1876.
18. Dubra A, Sulai Y. Reflective afocal broadband adaptive optics scanning ophthalmoscope. *Biomed Opt Express*. 2011;2:1757–1768.
19. Gray DC, Merigan W, Wolfing JI, et al. In vivo fluorescence imaging of primate retinal ganglion cells and retinal pigment epithelial cells. *Opt Express*. 2006;14:7144–7158.
20. Zhong Z, Petrig BL, Qi X, Burns SA. In vivo measurement of erythrocyte velocity and retinal blood flow using adaptive optics scanning laser ophthalmoscopy. *Opt Express*. 2008;16:12746–12756.
21. Martin JA, Roorda A. Pulsatility of parafoveal capillary leukocytes. *Exp Eye Res*. 2009;88:356–360.
22. Duncan JL, Zhang Y, Gandhi J, et al. High-resolution imaging with adaptive optics in patients with inherited retinal degeneration. *Invest Ophthalmol Vis Sci*. 2007;48:3283–3291.
23. Talcott KE, Ratnam K, Sundquist SM, et al. Longitudinal study of cone photoreceptors during retinal degeneration and in response to ciliary neurotrophic factor treatment. *Invest Ophthalmol Vis Sci*. 2011;52):2219–2226.
24. Choi SS, Doble N, Hardy JL, et al. In vivo imaging of the photoreceptor mosaic in retinal dystrophies and correlations with visual function. *Invest Ophthalmol Vis Sci*. 2006;47:2080–2092.
25. Wolfing JI, Chung M, Carroll J, Roorda A, Williams DR. High-resolution retinal imaging of cone-rod dystrophy. *Ophthalmology*. 2006;113:1019.e1.
26. Roorda A, Zhang Y, Duncan JL. High-resolution in vivo imaging of the RPE mosaic in eyes with retinal disease. *Invest Ophthalmol Vis Sci*. 2007;48:2297–2303.
27. Zayit-Soudry S, Duncan JL, Syed R, Menghini M, Roorda AJ. Cone structure imaged with adaptive optics scanning laser ophthalmoscopy in eyes with nonneovascular age-related macular degeneration. *Invest Ophthalmol Vis Sci*. 2013;54:7498–7509.
28. Rossi EA, Rangel-Fonseca P, Parkins K, et al. In vivo imaging of retinal pigment epithelium cells in age related macular degeneration. *Biomed Opt Express*. 2013;4:2527–2539.
29. Tam J, Dhamdhere KP, Tiruveedhula P, et al. Disruption of the retinal parafoveal capillary network in type 2 diabetes before the onset of diabetic retinopathy. *Invest Ophthalmol Vis Sci*. 2011;52:9257–9266.
30. Tam J, Dhamdhere KP, Tiruveedhula P, et al. Subclinical capillary changes in non-proliferative diabetic retinopathy. *Optom Vis Sci Off Publ Am Acad Optom*. 2012;89:E692–E703.
31. Burns SA, Elsner AE, Chui TY, et al. In vivo adaptive optics microvascular imaging in diabetic patients without clinically severe diabetic retinopathy. *Biomed Opt Express*. 2014;5:961–974.
32. Li KY, Roorda A. Automated identification of cone photoreceptors in adaptive optics retinal images. *J Opt Soc Am A Opt Image Sci Vis*. 2007;24:1358–1363.
33. Song H, Chui TYP, Zhong Z, Elsner AE, Burns SA. Variation of cone photoreceptor packing density with retinal eccentricity and age. *Invest Ophthalmol Vis Sci*. 2011;52:7376–7384.
34. Chui TYP, Song H, Clark CA, Papay JA, Burns SA, Elsner AE. Cone photoreceptor packing density and the outer nuclear layer thickness in healthy subjects. *Invest Ophthalmol Vis Sci*. 2012;53:3545–3553.

Investigative Ophthalmology & Visual Science

35. Rangel-Fonseca P, Gómez-Vieyra A, Malacara-Hernández D, Wilson MC, Williams DR, Rossi EA. Automated segmentation of retinal pigment epithelium cells in fluorescence adaptive optics images. *J Opt Soc Am A*. 2013;30:2595.
36. Tam J, Tiruveedhula P, Roorda A. Characterization of single-file flow through human retinal parafoveal capillaries using an adaptive optics scanning laser ophthalmoscope. *Biomed Opt Express*. 2011;2:781–793.
37. Schallek J, Schwarz C, Williams D. Rapid, automated measurements of single cell blood velocity in the living eye. *Invest Ophthalmol Vis Sci*. 2013;54:398–398.
38. Tuten WS, Tiruveedhula P, Roorda A. Adaptive optics scanning laser ophthalmoscope-based microperimetry. *Optom Vis Sci Off Publ Am Acad Optom*. 2012;89:563–574.
39. Wang Q, Tuten WS, Lujan BJ, et al. Adaptive optics microperimetry and OCT images show preserved function and recovery of cone visibility in macular telangiectasia type 2 retinal lesions. *Invest Ophthalmol Vis Sci*. 2015;56:778–786.
40. Vilupuru AS, Rangaswamy NV, Frishman LJ, Smith EL, Harwerth RS, Roorda A. Adaptive optics scanning laser ophthalmoscopy for in vivo imaging of lamina cribrosa. *J Opt Soc Am A Opt Image Sci Vis*. 2007;24:1417–1425.
41. Ivers KM, Sredar N, Patel NB, et al. High-resolution longitudinal examination of the lamina cribrosa and optic nerve head in living non-human primates with experimental glaucoma. *Invest Ophthalmol Vis Sci*. 2012;53:3697–3697.
42. Takayama K, Ooto S, Hangai M, et al. High-resolution imaging of the retinal nerve fiber layer in normal eyes using adaptive optics scanning laser ophthalmoscopy. *PLoS One*. 2012;7:e33158.
43. Scoles D, Higgins BP, Cooper RF, et al. Microscopic inner retinal hyper-reflective phenotypes in retinal and neurologic disease. *Invest Ophthalmol Vis Sci*. 2014;55:4015–4029.
44. Chance B, Cohen P, Jobsis F, Schoener B. Intracellular oxidation-reduction states in vivo. *Science*. 1962;137:499–508.
45. Delori FC, Dorey CK, Staurenghi G, Arend O, Goger DG, Weiter JJ. In vivo fluorescence of the ocular fundus exhibits retinal pigment epithelium lipofuscin characteristics. *Invest Ophthalmol Vis Sci*. 1995;36:718–729.
46. Imanishi Y, Gerke V, Palczewski K. Retinosomes: new insights into intracellular managing of hydrophobic substances in lipid bodies. *J Cell Biol*. 2004;166:447–453.
47. Palczewska G, Maeda T, Imanishi Y, et al. Noninvasive multiphoton fluorescence microscopy resolves retinol and retinal condensation products in mouse eyes. *Nat Med*. 2010;16:1444–1449.
48. Sparrow JR, Wu Y, Nagasaki T, Yoon KD, Yamamoto K, Zhou J. Fundus autofluorescence and the bisretinoids of retina. *Photochem Photobiol Sci Off J Eur Photochem Assoc Eur Soc Photobiol*. 2010;9:1480–1489.
49. Richards-Kortum R, Sevick-Muraca E. Quantitative optical spectroscopy for tissue diagnosis. *Annu Rev Phys Chem*. 1996;47:555–606.
50. Harrison DE, Chance B. Fluorimetric technique for monitoring changes in the level of reduced nicotinamide nucleotides in continuous cultures of microorganisms. *Appl Microbiol*. 1970;19:446–450.
51. Travis GH, Golczak M, Moise AR, Palczewski K. Diseases caused by defects in the visual cycle: retinoids as potential therapeutic agents. *Annu Rev Pharmacol Toxicol*. 2007;47:469–512.
52. Wagenseil JE, Mecham RP. Elastin in large artery stiffness and hypertension. *J Cardiovasc Transl Res*. 2012;5:264–273.
53. Dillon J, Zheng L, Merriam JC, Gaillard ER. Transmission spectra of light to the mammalian retina. *Photochem Photobiol*. 2007;71:225–229.
54. Denk W, Strickler JH, Webb WW. Two-photon laser scanning fluorescence microscopy. *Science*. 1990;248:73–76.
55. Lu R-W, Li Y-C, Ye T, et al. Two-photon excited autofluorescence imaging of freshly isolated frog retinas. *Biomed Opt Express*. 2011;2:1494–1503.
56. Gualda EJ, Bueno JM, Artal P. Wavefront optimized nonlinear microscopy of ex vivo human retinas. *J Biomed Opt*. 2010;15:026007.
57. Palczewska G, Golczak M, Williams DR, Hunter JJ, Palczewski K. Endogenous fluorophores enable two-photon imaging of the primate eye. *Invest Ophthalmol Vis Sci*. 2014;55:4438–4447.
58. Masihzadeh O, Lei TC, Ammar DA, Kahook MY, Gibson EA. A multiphoton microscope platform for imaging the mouse eye. *Mol Vis*. 2012;18:1840–1848.
59. Kusnyerik A, Rozsa B, Veress M, Szabo A, Nemeth J, Maak P. Modeling of in vivo acousto-optic two-photon imaging of the retina in the human eye. *Opt Express*. 2015;23:23436.
60. Hunter JJ, Masella B, Dubra A, et al. Images of photoreceptors in living primate eyes using adaptive optics two-photon ophthalmoscopy. *Biomed Opt Express*. 2011;2:139–148.
61. Sharma R, Yin L, Geng Y, et al. In vivo two-photon imaging of the mouse retina. *Biomed Opt Express*. 2013;4:1285–1293.
62. Sharma R, Schwarz C, Williams DR, Palczewska G, Palczewska K, Hunter JJ. In vivo two-photon fluorescence kinetics of primate rods and cones. *Invest Ophthalmol Vis Sci*. 2016;57:647–657.
63. Sheppard CJR, Gu M. Image formation in two-photon fluorescence microscopy. *Opt - Int J Light Electron Opt*. 1990;86:104–106.
64. Gu M, Sheppard CJR. Effects of a finite-sized pinhole on 3D image formation in confocal two-photon fluorescence microscopy. *J Mod Opt - J MOD Opt*. 1993;40:2009–2024.
65. Richards B, Wolf E. Electromagnetic diffraction in optical systems. II. Structure of the image field in an aplanatic system. *Proc R Soc Lond Math Phys Eng Sci*. 1959;253:358–379.
66. Zipfel WR, Williams RM, Webb WW. Nonlinear magic: multiphoton microscopy in the biosciences. *Nat Biotech*. 2003;21:1369–1377.
67. Dubra A, Harvey Z. Registration of 2D images from fast scanning ophthalmic instruments. In: *Proceedings of the 4th International Conference on Biomedical Image Registration*. WBIR'10. Berlin, Heidelberg: Springer-Verlag; 2010:60–71.
68. Yang Q, Zhang J, Nozato K, et al. Closed-loop optical stabilization and digital image registration in adaptive optics scanning light ophthalmoscopy. *Biomed Opt Express*. 2014;5:3174.
69. Fine BS, Zimmerman LE. Muller's cells and the "middle limiting membrane" of the human retina. An electron microscopic study. *Invest Ophthalmol*. 1962;1:304–326.
70. Hogan MJ, Alvarado JA, Weddell JE. *Histology of the Human Eye: An Atlas and Textbook*. Philadelphia, PA: Saunders; 1971.
71. Radius RL, Anderson DR. The histology of retinal nerve fiber layer bundles and bundle defects. *Arch Ophthalmol*. 1979;97:948–950.
72. Ramírez JM, Triviño A, Ramírez AI, Salazar JJ, García-Sánchez J. Structural specializations of human retinal glial cells. *Vision Res*. 1996;36:2029–2036.
73. Wong LC, Langille BL. Developmental remodeling of the internal elastic lamina of rabbit arteries: effect of blood flow. *Circ Res*. 1996;78:799–805.
74. Zoumi A, Lu X, Kassab GS, Tromberg BJ. Imaging coronary artery microstructure using second-harmonic and two-

Investigative Ophthalmology & Visual Science

photon fluorescence microscopy. *Biophys J*. 2004;87:2778–2786.

75. Zoumi A, Yeh A, Tromberg BJ. Imaging cells and extracellular matrix in vivo by using second-harmonic generation and two-photon excited fluorescence. *Proc Natl Acad Sci U S A*. 2002;99:11014–11019.
76. Zipfel WR, Williams RM, Christie R, Nikitin AY, Hyman BT, Webb WW. Live tissue intrinsic emission microscopy using multiphoton-excited native fluorescence and second harmonic generation. *Proc Natl Acad Sci U S A*. 2003;100:7075–7080.
77. Arribas SM, Daly CJ, González MC, McGrath JC. Imaging the vascular wall using confocal microscopy. *J Physiol*. 2007;584:5–9.
78. Stitt A. Advanced glycation: an important pathological event in diabetic and age related ocular disease. *Br J Ophthalmol*. 2001;85:746–753.
79. Tseng J-Y, Ghazaryan AA, Lo W, et al. Multiphoton spectral microscopy for imaging and quantification of tissue glycation. *Biomed Opt Express*. 2010;2:218–230.
80. Curcio CA, Allen KA. Topography of ganglion cells in human retina. *J Comp Neurol*. 1990;300:5–25.
81. Snodderly DM, Weinhaus RS, Choi JC. Neural-vascular relationships in central retina of macaque monkeys (Macaca fascicularis). *J Neurosci Off J Soc Neurosci*. 1992;12:1169–1193.
82. Schweitzer D, Schenke S, Hammer M, et al. Towards metabolic mapping of the human retina. *Microsc Res Tech*. 2007;70:410–419.
83. Peters S, Hammer M, Schweitzer D. Two-photon excited fluorescence microscopy application for ex vivo investigation of ocular fundus samples. *Proc SPIE*. 2011;8086:808605–808605.
84. Kageyama GH, Wong-Riley MT. The histochemical localization of cytochrome oxidase in the retina and lateral geniculate nucleus of the ferret, cat, and monkey, with particular reference to retinal mosaics and ON/OFF-center visual channels. *J Neurosci Off J Soc Neurosci*. 1984;4:2445–2459.
85. Lipton P. Effects of membrane depolarization on nicotinamide nucleotide fluorescence in brain slices. *Biochem J*. 1973;136:999–1009.
86. Kasischke KA, Vishwasrao HD, Fisher PJ, Zipfel WR, Webb WW. Neural activity triggers neuronal oxidative metabolism followed by astrocytic glycolysis. *Science*. 2004;305:99–103.
87. Hurley JB, Lindsay KJ, Du J. Glucose, lactate, and shuttling of metabolites in vertebrate retinas. *J Neurosci Res*. 2015;93:1079–1092.
88. Mecham RP. Overview of Extracellular Matrix. In: *Current Protocols in Cell Biology*. New York, NY: John Wiley & Sons, Inc.; 2001.
89. Halper J, Kjaer M. Basic components of connective tissues and extracellular matrix: elastin, fibrillin, fibulins, fibrinogen, fibronectin, laminin, tenascins and thrombospondins. *Adv Exp Med Biol*. 2014;802:31–47.
90. Enoch JM. Optical properties of the retinal receptors. *J Opt Soc Am*. 1963;53:71.
91. Liu Z, Kocaoglu OP, Turner TL, Miller DT. Modal content of living human cone photoreceptors. *Biomed Opt Express*. 2015;6:3378.
92. Bindewald-Wittich A, Han M, Schmitz-Valckenberg S, et al. Two-photon-excited fluorescence imaging of human RPE cells with a femtosecond Ti:Sapphire laser. *Invest Ophthalmol Vis Sci*. 2006;47:4553–4557.
93. Palczewska G, Dong Z, Golczak M, et al. Noninvasive two-photon microscopy imaging of mouse retina and retinal pigment epithelium through the pupil of the eye. *Nat Med*. 2014;20:785–789.
94. Morgan J, Dubra A, Wolfe R, Merigan WH, Williams DR. In vivo autofluorescence imaging of the human and macaque retinal pigment epithelial cell mosaic. *Invest Ophthalmol Vis Sci*. 2009;50:1350–1359.
95. Boyer NP, Higbee D, Currin MB, et al. Lipofuscin and N-retinylidene-N-retinylethanolamine (A2E) accumulate in retinal pigment epithelium in absence of light exposure: their origin is 11-cis-retinal. *J Biol Chem*. 2012;287:22276–22286.
96. Padayatti P, Palczewska G, Sun W, Palczewski K, Salom D. Imaging of protein crystals with two-photon microscopy. *Biochemistry (Mosc)*. 2012;51:1625–1637.
97. Ragauskaite L, Heckathorn RC, Gaillard ER. Environmental effects on the photochemistry of A2-E, a component of human retinal lipofuscin. *Photochem Photobiol*. 2001;74:483–488.
98. ANSI. American National Standard for Safe Use of Lasers ANSI Z136.1-2014. 2014.
99. Chao TI, Skachkov SN, Eberhardt W, Reichenbach A. Na+ channels of Müller (glial) cells isolated from retinae of various mammalian species including man. *Glia*. 1994;10:173–185.
100. Bringmann A, Pannicke T, Grosche J, et al. Müller cells in the healthy and diseased retina. *Prog Retin Eye Res*. 2006;25:397–424.
101. Powner MB, Gillies MC, Zhu M, Vevis K, Hunyor AP, Fruttiger M. Loss of Müller's cells and photoreceptors in macular telangiectasia type 2. *Ophthalmology*. 2013;120:2344–2352.
102. Litts KM, Messinger JD, Freund KB, Zhang Y, Curcio CA. Inner segment remodeling and mitochondrial translocation in cone photoreceptors in age-related macular degeneration with outer retinal tubulation. *Invest Ophthalmol Vis Sci*. 2015;56:2243–2253.
103. Chen C, Tsina E, Cornwall MC, Crouch RK, Vijayaraghavan S, Koutalos Y. Reduction of all-trans retinal to all-trans retinol in the outer segments of frog and mouse rod photoreceptors. *Biophys J*. 2005;88:2278–2287.
104. Staurenghi G, Sadda S, Chakravarthy U, Spaide RF. International Nomenclature for Optical Coherence Tomography (IN•OCT) Panel. Proposed lexicon for anatomic landmarks in normal posterior segment spectral-domain optical coherence tomography: the IN•OCT consensus. *Ophthalmology*. 2014;121:1572–1578.

Investigative Ophthalmology & Visual Science